



Article

Tuning of Structural, Dielectric, and Electronic Properties of Cu Doped Co–Zn Ferrite Nanoparticles for Multilayer Inductor Chip Applications

Muhammad Hadi ¹, Khalid Mujasam Batoo ^{2,*} , Ankush Chauhan ³, Omar M. Aldossary ¹ , Ritesh Verma ³ and Yujie Yang ⁴

- ¹ Department of Physics and Astronomy, College of Science, King Saud University, P.O. Box 2455, Riyadh 11451, Saudi Arabia; mhtghamdi@gmail.com (M.H.); omar@ksu.edu.sa (O.M.A.)
² King Abdullah Institute for Nanotechnology, King Saud University, P.O. Box 2455, Riyadh 11451, Saudi Arabia
³ School of Physics and Materials Science, Shoolini University of Biotechnology & Management Sciences, Bajhol, Solan 173212, India; ankushchauhan18@gmail.com (A.C.); vermaritesh@gmail.com (R.V.)
⁴ Engineering Technology Research Center of Magnetic Materials, Anhui Province, School of Physics & Materials Science, Anhui University, Hefei 230601, China; loyalty-yyj@163.com
* Correspondence: kbatoo@ksu.edu.sa



Citation: Hadi, M.; Batoo, K.M.; Chauhan, A.; Aldossary, O.M.; Verma, R.; Yang, Y. Tuning of Structural, Dielectric, and Electronic Properties of Cu Doped Co–Zn Ferrite Nanoparticles for Multilayer Inductor Chip Applications. *Magnetochemistry* **2021**, *7*, 53. <https://doi.org/10.3390/magnetochemistry7040053>

Academic Editors: David S. Schmooll, Gopalu Karunakaran, Raji Govindan and Govindan Suresh Kumar

Received: 12 March 2021

Accepted: 13 April 2021

Published: 14 April 2021

Publisher's Note: MDPI stays neutral with regard to jurisdictional claims in published maps and institutional affiliations.



Copyright: © 2021 by the authors. Licensee MDPI, Basel, Switzerland. This article is an open access article distributed under the terms and conditions of the Creative Commons Attribution (CC BY) license (<https://creativecommons.org/licenses/by/4.0/>).

Abstract: Herein, we report the synthesis of nanoparticles and doping of Cu-doped Co–Zn ferrites using the auto-combustion sol–gel synthesis technique. X-ray diffraction studies confirmed the single-phase structure of the samples with space group $Fd\bar{3}m$ and crystallite size in the range of 20.57–32.69 nm. Transmission electron microscopy micrographs and selected area electron diffraction patterns confirmed the polycrystalline nature of the ferrite nanoparticles. Energy-dispersive X-ray spectroscopy revealed the elemental composition in the absence of any impurity phases. Fourier-transform infrared studies showed the presence of two prominent peaks at approximately 420 cm^{-1} and 580 cm^{-1} , showing metal–oxygen stretching and the formation of ferrite composite. X-ray photoelectron spectroscopy was employed to determine the oxidation states of Fe, Co, Zn, and Cu and O vacancies based on which cationic distributions at tetrahedral and octahedral sites are proposed. Dielectric spectroscopy showed that the samples exhibit Maxwell–Wagner interfacial polarization, which decreases as the frequency of the applied field increases. The dielectric loss of the samples was less than 1, confirming that the samples can be used for the fabrication of multilayer inductor chips. The ac conductivity of the samples increased with increasing doping and with frequency, and this has been explained by the hopping model. The hysteresis loops revealed that coercivity decreases slightly with doping, while the highest saturation magnetization of 55.61 emu/g was obtained when $x = 0.1$. The magnetic anisotropic constant was found to be less than 0.5, which suggests that the samples exhibit uniaxial anisotropy rather than cubic anisotropy. The squareness ratio indicates that the samples are useful in high-frequency applications.

Keywords: nanoparticles; ferrites; XRD; SEM; XPS; VSM

1. Introduction

Nanoparticles exhibit novel material properties because of their small particle size, which differs from the bulk solid state. Many reports have shown that the evolution of metallic particle properties depends on their size [1,2]. Ferrites have attracted considerable attention in the scientific community over the past few decades because of their unique and promising electrical, optical, and magnetic properties. Ferrites are one of the good dielectric materials, which have low conductivity or high resistivity that make them an appropriate choice for various applications in devices such as microwave devices, transformers, electric generators, and storage devices [3]. Among the various spinel ferrites that have important properties, cobalt ferrite (CoFe_2O_4) has been the center of attention and the subject of much

interest. It has been studied extensively by the scientific community because of its high coercivity, moderate saturation magnetization, high chemical stability, and magnetic and electrical conductivity [4,5].

CoFe₂O₄ possesses an inverse spinel structure, while ZnFe₂O₄ has a normal spinel structure. Substituting Co for Zn in CoFe₂O₄ results in a deformed spinel structure depending on the ratio of Co:Zn within the precursor solutions [6]. It is more interesting to substitute magnetic Co²⁺ ions with non-magnetic Zn²⁺ in Co-ferrite to understand the difference in the properties of the new system. Spinel ferrites have a general formula AB₂O₄, where A = Zn, Co, Mg, Mn, etc., in which the metal cations A and B represent tetrahedral and octahedral sites [7]. In a spinel ferrite, 8 tetrahedral sites are occupied by divalent cations and 16 octahedral sites are occupied by trivalent cations. This type of ferrite has attracted considerable attention in the scientific community because of its wide range of applications in various fields, from the biomedical to electronic industries and for uses such as in magneto-optical devices [8], a contrast agent for magnetic resonance imaging (MRI) [9], drug delivery systems [10], spintronic devices [11], and magneto hyperthermia [12]. Halder et al. studied the influence of the annealing temperature and concentration of the Co_{0.5}Zn_{0.5}Fe₂O₄ nanoparticles as a heat generation material for hyperthermia therapy and found that all the samples possessed a single-phase cubic spinel structure [13]. Feng et al. synthesized Co_xZn_{1-x}Fe₂O₄ by employing an auto-combustion route, and the XRD patterns showed a single-phase cubic spinel structure. The M–H curves showed superparamagnetic behavior at room temperature [14]. Köseoğlu et al. studied the Co_xZn_{1-x}Fe₂O₄ nanocrystals and reported that the sample has a large grain structure, and the value of magnetization sharply increases with an applied magnetic field [15]. Cu²⁺ is a highly electrically conductive Jahn-Teller ion in the ground state with degenerate orbitals that are influenced by the distortion. The crystal distortions are caused by the incorporation of Cu²⁺ ions in the spinel ferrites, which is directly linked with enhancement in electrical and magnetic properties [16–18]. It has been reported that the crystal distortion caused by Cu²⁺ ions depend on their occupancy at tetrahedral and octahedral sites [19].

Multilayer chip inductors (MLCIs) are the major component of radio-frequency circuits in electronic devices required for the amplification of signals, filtration, and modulation [20]. The main requirement of MLCIs is a high permeability value for the reduced number of layers in the chip for enhancing the miniaturization of electronic devices [21]. The soft ferrite materials are co-fired layer by layer with internal contact materials [22]. Electromagnetic interference (EMI) is a major threat to human health, it also affects the functionality of electronic devices. The synergetic effect of magnetic and dielectric loss influences the microwave absorption properties of ferrites and is composition-dependent [23,24].

Gurusiddesh et al. investigated the microwave absorption properties of polyalanine-decorated CoFe₂O₄ nanoparticles with shielding effectiveness values of 39.9 dB and 58.22 dB at 50 Hz for pure and polyalanine-decorated CoFe₂O₄ nanoparticles, respectively [25]. Sulaiman et al. observed that at a 1:1 concentration of Co_{0.5}Zn_{0.5}Fe₂O₄/PANI-PTSA, reflection losses were −2.3 dB (>40% power absorption) at 8.1 GHz, −17.08 dB (98% power absorption) at 9 GHz, and −24.86 dB (99.73% power absorption) at 10.9 GHz, revealing its potential as a microwave absorbing material [26].

Various methods have been adopted to synthesize cobalt–zinc ferrite nanoparticles, such as co-precipitation, sol–gel, solid-state, micro-emulsions, combustion, and hydrothermal methods. Among the different chemical methods reported in the literature used to synthesize Co–Zn ferrite nanoparticles, the sol–gel process is likely an effective method, which results in inhomogeneous and crystalline nanoparticles. The sol–gel auto-combustion method is a low-temperature synthesis process, which involves the hydrolysis and condensation reactions of metal precursors, prompting the arrangement of a three-dimensional inorganic system [27]. In this paper, we report the structural, morphological, electronic, and dielectric properties of the Cu-substituted Co–Zn ferrites prepared by the sol–gel auto-combustion method for MLCI and EMI filter applications.

2. Materials and Method

2.1. Materials

All the chemicals used to synthesize the nanoparticles of Cu-doped Co–Zn ferrite were of analytical grade (AR) and were used without any further purification. The chemicals used in the fabrication of the ferrites included cobalt nitrate hexahydrate ($\text{Co}(\text{NO}_3)_2 \cdot 6\text{H}_2\text{O}$), ferric nitrate hexahydrate ($\text{Fe}(\text{NO}_3)_3 \cdot 9\text{H}_2\text{O}$), zinc nitrate hexahydrate ($\text{Zn}(\text{NO}_3)_2 \cdot 6\text{H}_2\text{O}$), copper nitrate hexahydrate ($\text{Cu}(\text{NO}_3)_2 \cdot 6\text{H}_2\text{O}$), citric acid ($\text{C}_6\text{H}_8\text{O}_7 \cdot \text{H}_2\text{O}$), ethylene glycol ($\text{C}_2\text{H}_6\text{O}_2$), and ammonia ($\text{NH}_3 \cdot \text{H}_2\text{O}$). Triple distilled water was used for the synthesis of the Co–Zn ferrite nanoparticles.

2.2. Method

Copper ion-substituted Co–Zn ferrite powders with a general formula of $\text{Co}_{0.5}\text{Zn}_{0.5}\text{Fe}_{2-x}\text{Cu}_x\text{O}_4$ (where, $x = 0.0, 0.5, 0.1, \text{ and } 0.05$, respectively) were synthesized using the sol–gel auto-combustion method. The ratio of a chelating agent, citric acid, to metal nitrate was 1:1. First, the stoichiometric weight of ($\text{Co}(\text{NO}_3)_2 \cdot 6\text{H}_2\text{O}$), ($\text{Zn}(\text{NO}_3)_2 \cdot 6\text{H}_2\text{O}$), ($\text{Cu}(\text{NO}_3)_2 \cdot 6\text{H}_2\text{O}$), ($\text{Fe}(\text{NO}_3)_3 \cdot 9\text{H}_2\text{O}$), and ($\text{C}_6\text{H}_8\text{O}_7 \cdot \text{H}_2\text{O}$) were individually dissolved in deionized water for a hydrolysis reaction at $60\text{ }^\circ\text{C}$ with continuous stirring for 45 min. Ammonia solution was added dropwise to maintain the pH value at 7. After some time, ethylene glycol (gelating reagent) was added to the solution as a polymerization promoter; the solution began to turn into a brown gel, which was heated at $80\text{ }^\circ\text{C}$ under continuous stirring for 3 h. The gel was dried at $120\text{ }^\circ\text{C}$, and a self-propagating combustion process occurred, in which most of the organic solvents were burned and an almost-black powder was left. The powder was calcined at $400\text{ }^\circ\text{C}$ for 12 h and then milled using a mortar and pestle for 30 min. The samples were pressed to circular disk-shaped pellets with opposite sides coated with a silver paste to create a parallel plate capacitor geometry for the dielectric measurements.

2.3. Characterization

The structure and crystallite sizes of the as-prepared nanoparticles (NPs) were characterized by X-ray diffraction (XRD, Rigaku Miniflex-600, Japan), with $\text{CuK}\alpha$ radiation ($\lambda = 1.5405\text{ \AA}$) between 20° and 80° at a scanning rate of $2^\circ/\text{min}$ at room temperature. The surface morphology was studied using a field emission scanning electron microscope (FESEM, JSM 7600F JEOL, Japan). The cross-sections and particle sizes of the nanoparticles were studied using a field emission transmission electron microscope (FETEM, JEM-2100F, JEOL, Japan) coupled with energy-dispersive X-ray (EDX) analysis, operating at an accelerating voltage of 200 kV. Fourier-transform infrared (FTIR) spectroscopy measurements were carried out using a Perkin-Elmer 580B IR spectrometer by the KBr pellet technique. X-ray photoelectron spectroscopy (XPS) measurements were carried out using a Sigma 2 XPS and a ThetaProbe manufactured by Thermo Fisher Scientific Inc., East Grinstead, UK. Sigma 2 was equipped with an Al/Mg Ka twin source. Dielectric measurements were carried out using the HIOKI LCR meter IM3536 model.

3. Results and Discussion

3.1. XRD

The XRD patterns of the calcined $\text{Co}_{0.5}\text{Zn}_{0.5}\text{Fe}_{2-x}\text{Cu}_x\text{O}_4$ ferrites are given in Figure 1. The peaks are indexed as (220), (311), (222), (400), (422), (511), and (440) corresponding to the angular positions of $30^\circ, 35.6^\circ, 37.2^\circ, 43.3^\circ, 53.7^\circ, 57.2^\circ$, and 62.8° 2θ values, respectively, and they correspond to the standard peaks of CoFe_2O_4 with JCPDS file no. 22-1086. The XRD patterns revealed that all the samples possessed single-phase cubic spinel structures with a $Fd\bar{3}m$ space group, with an impurity phase of copper oxide at a higher concentration JCPDS file no. 05-0661 ruling out the formation of any unwanted secondary phases corresponding to any structure. The average crystallite size (D) was estimated using the Debye–Scherrer formula [28]:

$$D = 0.9\lambda/\beta\cos\theta, \quad (1)$$

where λ is the XRD wavelength (1.54 Å), θ is the diffraction angle, and β is the full-width half maximum of the diffraction peaks. It can be observed from Table 1 that the crystallite size decreases with the increase in the Cu^{2+} concentration. The XRD peak broadening was attributed to the small crystallite size and the generation of an intrinsic microstrain. The microstrain was produced due to the changes in the lattice parameter, which resulted from the crystal imperfections and dislocations. Hence, the microstrain that developed inside the crystal was calculated by the Williamson–Hall method based on the uniform deformation model (UDM) given by the straight-line equation [29]:

$$\beta \cos \theta = \frac{K\lambda}{D} + \varepsilon (4\sin \theta). \quad (2)$$

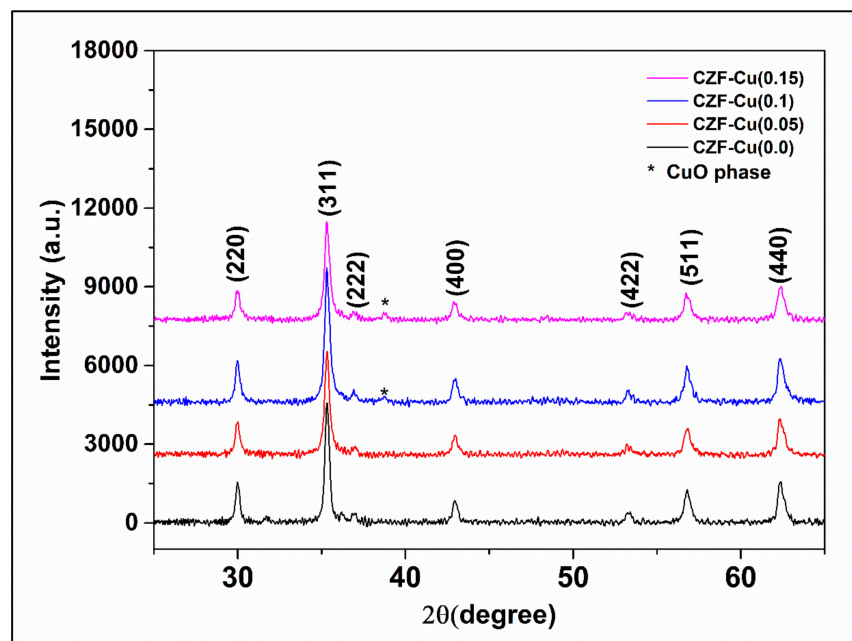


Figure 1. XRD patterns of $\text{Co}_{0.5}\text{Zn}_{0.5}\text{Cu}_x\text{Fe}_{2-x}\text{O}_4$.

Table 1. Structural parameters of $\text{Co}_{0.5}\text{Zn}_{0.5}\text{Fe}_{2-x}\text{Cu}_x\text{O}_4$ ferrites.

$\text{Co}_{0.5}\text{Zn}_{0.5}\text{Fe}_{2-x}\text{Cu}_x\text{O}_4$	$x = 0.0$	$x = 0.05$	$x = 0.1$	$x = 0.15$
Lattice constant "a" (Å)	8.4032	8.3961	8.4024	8.3651
Crystallite size D_{scherrer} (nm)	24.43	23.19	22.6	22.23
Strain(ε)	0.00187	0.0036	0.0036	0.0036
Volume (Å) ³	593.38	591.87	593.21	585.34
d_{AX} (Å)	1.9064	1.905	1.9064	1.8979
d_{BX} (Å)	2.052	2.0503	2.0518	2.0427
d_{AXE} (Å)	2.9801	3.1109	3.1132	3.0994
d_{BXE} (Å)	2.8283	2.8259	2.828	2.8155
d_{BXEU} (Å)	2.9726	2.9701	2.7809	2.9592
r_A (Å)	0.5866	0.5850	0.5864	0.5780
r_B (Å)	0.7303	0.7286	0.7301	0.721
L_A (Å)	3.6380	3.6356	3.6391	3.6221
L_B (Å)	2.9709	2.9684	2.9706	2.9575

The UDM model considers the isotropic nature of the crystals and the slope of the plot between $\beta\cos\theta$ along the y-axis and $4\sin\theta$ along the x-axis corresponding to each peak of the sample. It can be observed from Figure 2 that a nearly uniform strain is generated among all the samples as the Cu concentration increases, and correlation value R^2 is above 0.9, revealing a good fit. The values of lattice parameters a were calculated using the equation below [30] and are listed in Table 1:

$$a = d\sqrt{h^2 + k^2 + l^2} \quad (3)$$

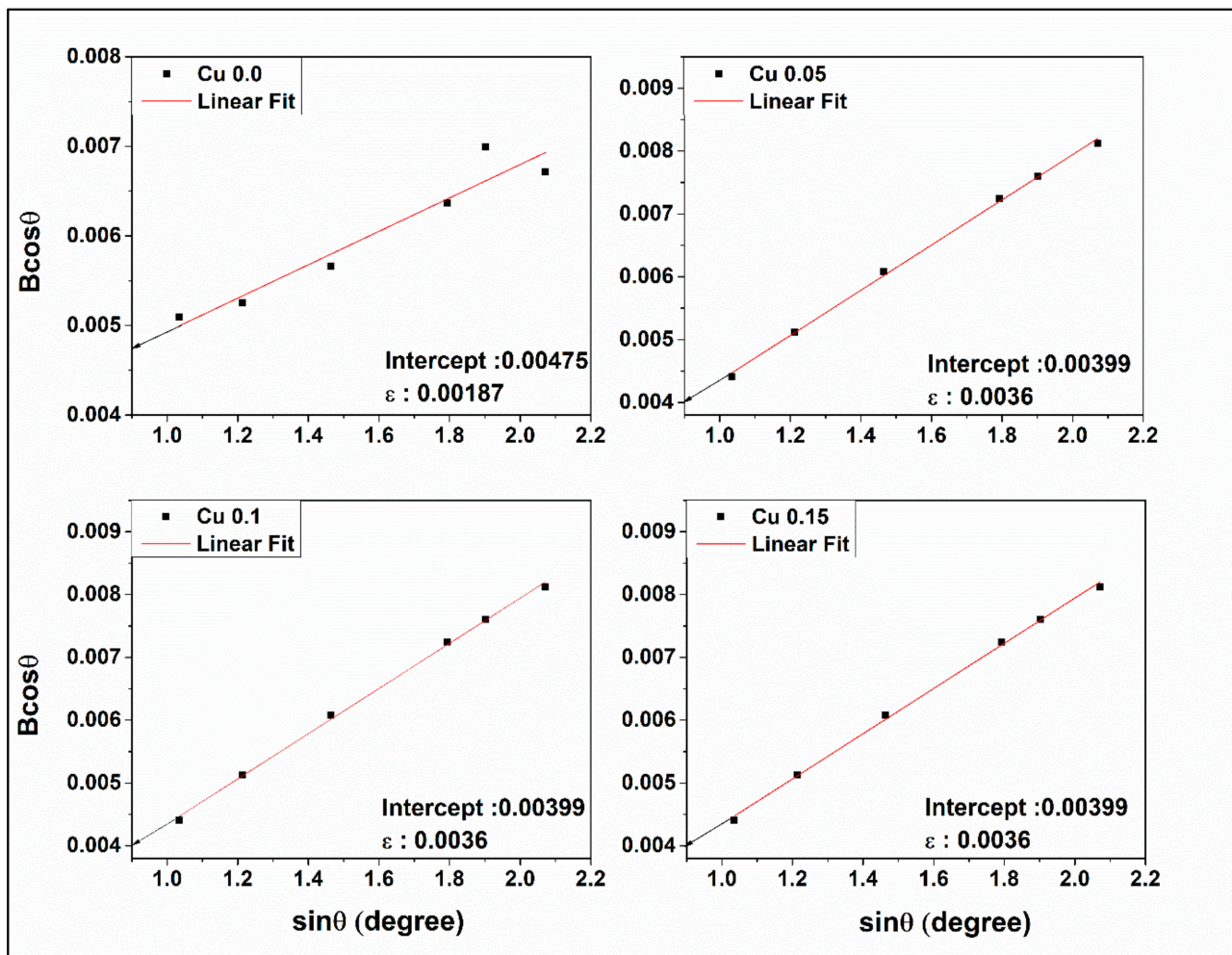


Figure 2. Williamson–Hall plot of $\text{Co}_{0.5}\text{Zn}_{0.5}\text{Fe}_{2-x}\text{Cu}_x\text{O}_4$.

The most accurate determination of the lattice parameter a given in Table 1 was employed using the Nelson–Riley plot shown in Figure 3 by plotting the lattice constant to the Nelson–Riley function $F(\theta)$ [31], given as:

$$F(\theta) = 1/2 \left[\cos\theta / \sin\theta + \cos\theta^2 / \theta \right] \quad (4)$$

The ionic radii of the tetrahedral (r_A) and octahedral (r_B) sites, hopping lengths L_A and L_B of the magnetic ions at the tetrahedral and octahedral sites, tetrahedral and octahedral bond lengths (d_{AX} and d_{BX}), tetrahedral edge length (d_{AXE}), and octahedral shared and unshared edge length (d_{BXE} and d_{BXEU}) were calculated using the following equations and are listed in Table 1 [32–34]:

$$d_{AX} = 1.732a(u - 0.25) \quad (5)$$

$$d_{BX} = a \sqrt{(3u - 2.75u + 0.6719)} \quad (6)$$

$$d_{AXE} = 1.4142a(2u - 0.5) \quad (7)$$

$$d_{BXE} = 1.4142a(1 - 2u) \quad (8)$$

$$d_{BXEU} = a \sqrt{(4u - 3u + 0.6875)} \quad (9)$$

$$r_A = (u - 0.25)a\sqrt{3} - R_0 \quad (10)$$

$$r_B = (0.625 - u)a - R_0 \quad (11)$$

$$LA = \left(\frac{\sqrt{3}}{4}\right)a \quad (12)$$

$$LB = \left(\frac{\sqrt{2}}{4}\right)a \quad (13)$$

where u is the oxygen parameter with the value of 0.381 Å and R_0 is 1.32 Å. Table 1 shows that there is a decrease in the above-mentioned values that is mainly due to the substitution of Cu^{+2} at the tetrahedral site instead of the octahedral site.

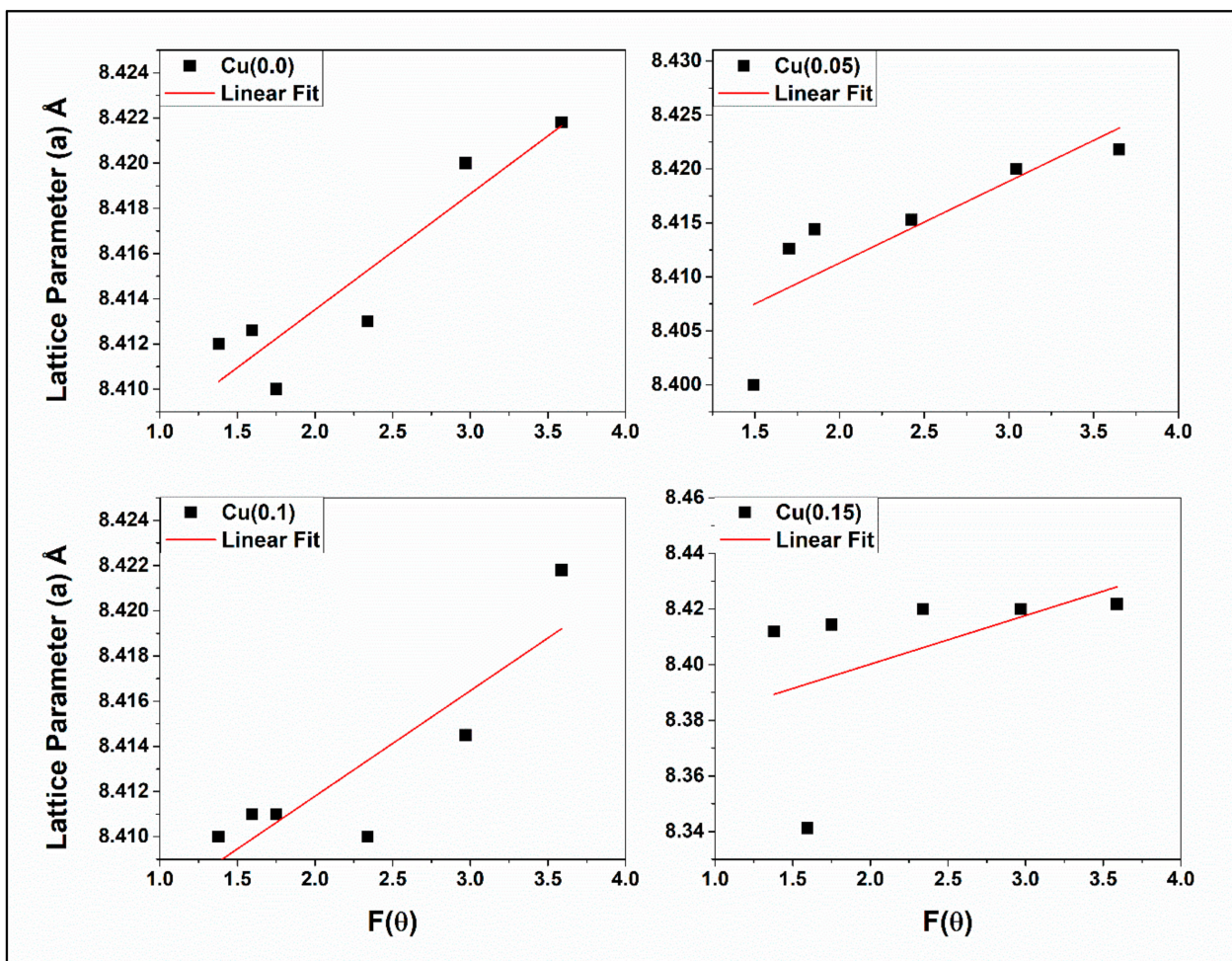


Figure 3. Nelson–Riley (N–R) plot of $\text{Co}_{0.5}\text{Zn}_{0.5}\text{Fe}_{2-x}\text{Cu}_x\text{O}_4$.

3.2. Morphology and EDX Analysis

The surface and cross-sectional morphology of the samples was studied using SEM and TEM. The SEM analysis showed that the samples were almost spherical but were agglomerated. The samples possessed a high percentage of porosity. The TEM analysis also

showed that the nanoparticles were almost spherical and were agglomerated. The average particle size distribution was estimated using image *J* software, shown in Figures 4b and 5b for the compositions $x = 0.0$ and 0.05. It was observed that the average particle size was between 20.57 nm and 32.69 nm. The average particle size decreased with the increase in the doping concentration, which showed that doping caused a decrease in the grain size. The selective area electron diffractions presented as insets in Figures 4a and 5b show dark and bright spots, which are signatures that confirm that the grown nanoparticles are highly crystalline in order.

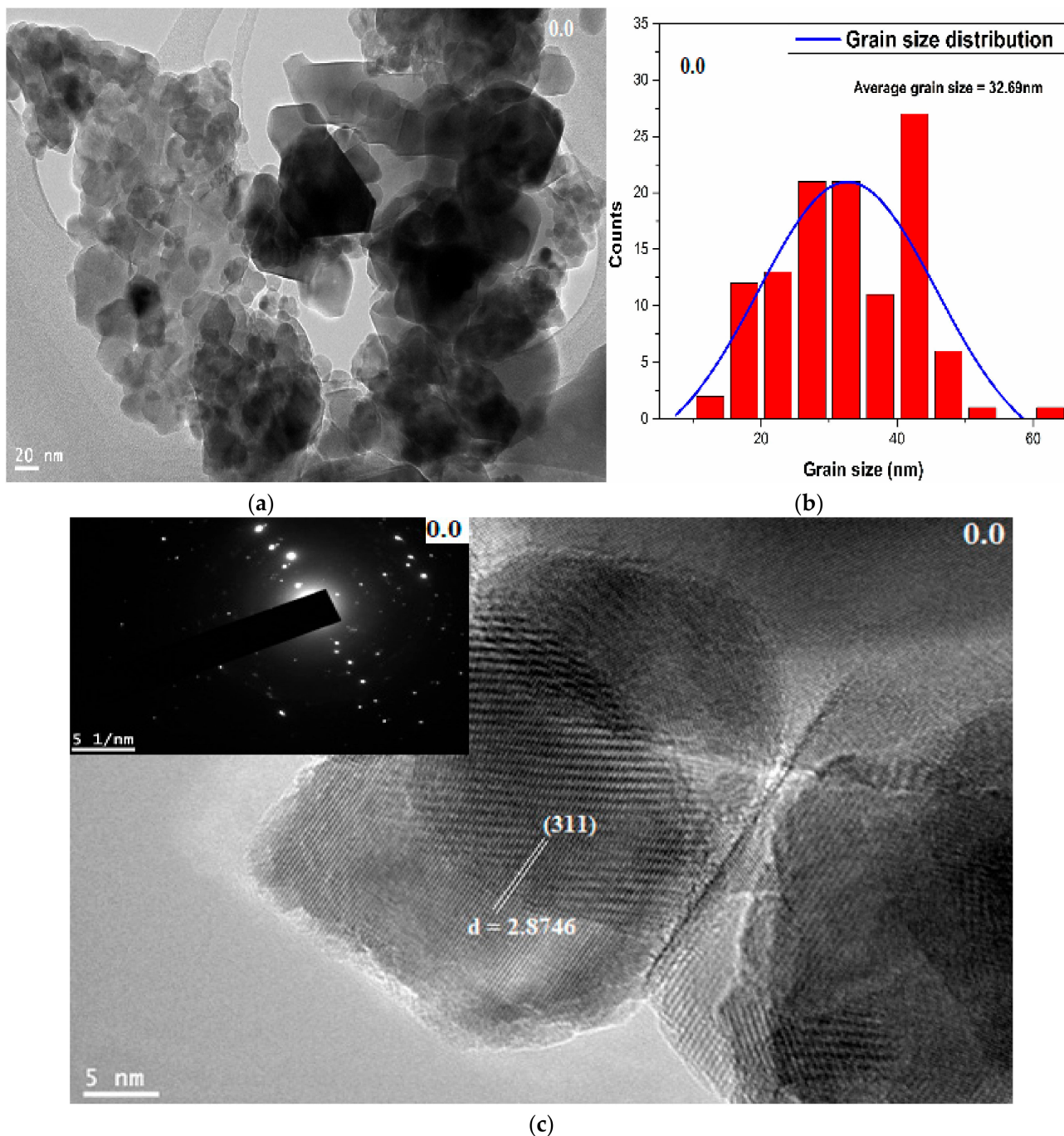


Figure 4. Shows (a) TEM micrograph, (b) grain size distribution, (c) lattice plane with inset showing SAED pattern for the composition $x = 0.0$.

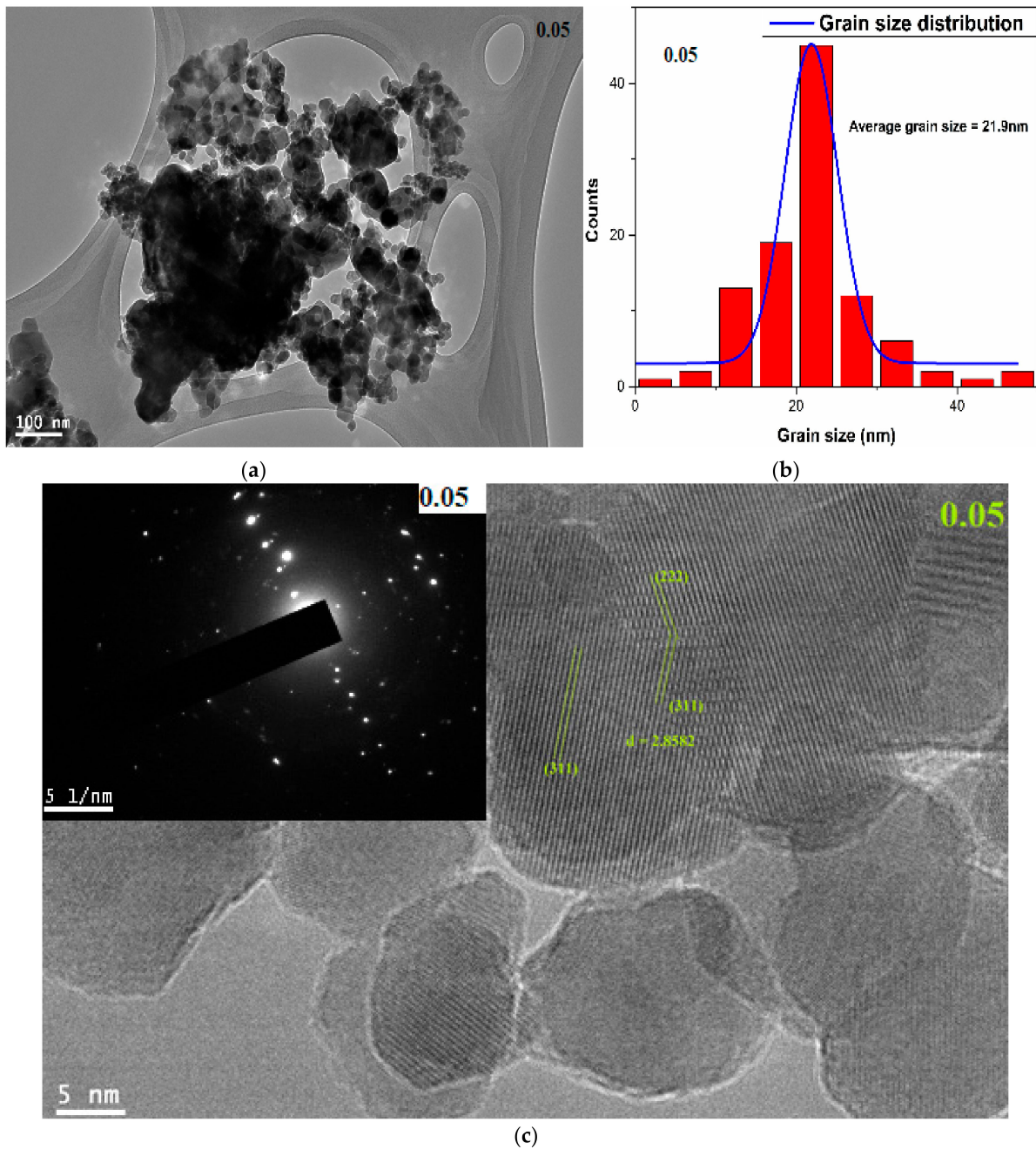


Figure 5. Shows (a) TEM micrograph, (b) grain size distribution, (c) lattice plane with inset showing SAED pattern for the composition $x = 0.05$.

The samples were further studied for the purity of the chemical composition through the EDX technique as shown in Figure 6a,b for the composition $x = 0.0$ and 0.05 . The peaks showed the presence of elements, such as Zn, Fe, Co, Fe, and O, which were the materials of the elements prepared, and hence, the presence of any secondary assay in the material was ruled out. Therefore, the elemental purity of the as-prepared samples was confirmed.

The peaks corresponding to the copper in the sample, $x = 0.0$, is due to the copper grid used in the TEM preparation. The distinction between the dopant copper and the copper grid can be visualized clearly from the intensity of the peak in the EDX pattern. A significant amount of carbon was also noted in the EDX pattern, which is quite normal as some residual carbon elements could be possible since we used a low sintering temperature to fire the sample.

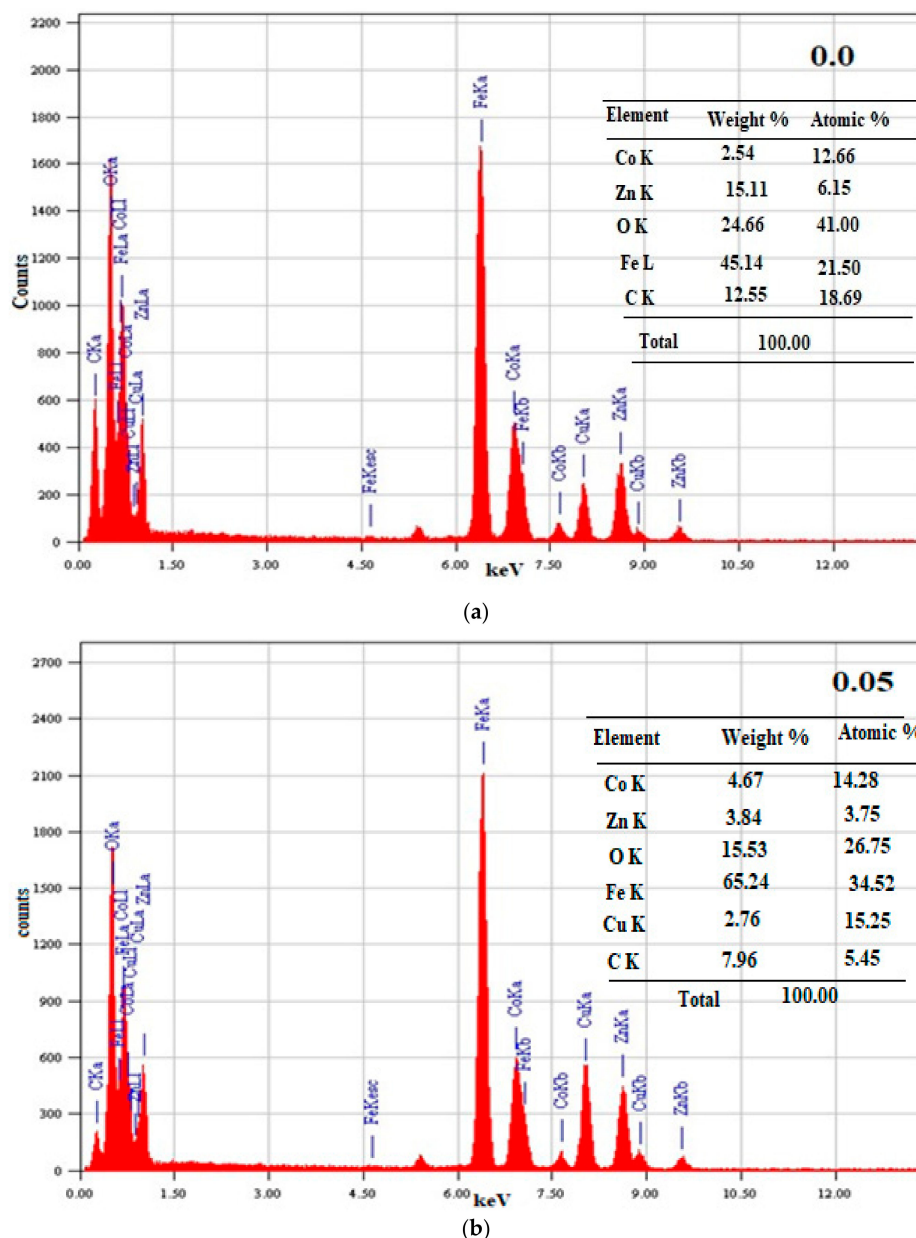


Figure 6. (a,b): EDX pattern for the composition $x = 0.0$ and 0.05 .

3.3. FTIR

The FTIR spectra of the Cu-doped ferrite nanoparticles were studied between the frequency range of $400\text{--}4000\text{ cm}^{-1}$, as is shown in Figure 7. Table 2 shows the transmittance frequencies observed for the samples during the measurement for the compositions. From the FTIR spectra, the formation of the various types of bonded crystals through ionic, covalent, or Van der Waals forces to the next lattice positions can be explained. The tetrahedral (A site) and octahedral (B site) positions in ferrites were occupied by metal ions for the geometrical configuration of the nearest oxygen positions. The broad frequency range between $3796\text{--}3788\text{ cm}^{-1}$ and $3377\text{--}3327\text{ cm}^{-1}$ represents the O–H stretch that corresponds to the –OH group attached to the metal oxide surface, which indicates that the water molecules were chemically adsorbed by the metal surface during the synthesis process. The vibrational modes observed in the frequency range of $580\text{--}588\text{ cm}^{-1}$ in the studied samples corresponded to Fe–O stretching at the octahedral site, while the modes present between 424 and 415 cm^{-1} represent the Fe–O stretching vibration at the tetrahedral site [35]. Notably, the vibrational modes at the tetrahedral site shifted towards the low-

frequency region with the Cu^{2+} ion doping, showing the contraction of the metal–oxygen bonds. Conversely, the bands at 580 cm^{-1} shifted towards the relatively high-frequency side with the doping, showing the stretching of the metal–oxygen bond. The O–H in the plane and out of plane bond appears at 1626 cm^{-1} to 1631 cm^{-1} , respectively. The presence of H_2O absorption bands in and out of the plane and metal–oxygen bonds confirms the existence of Ni and Cu in the synthesized samples [36,37].

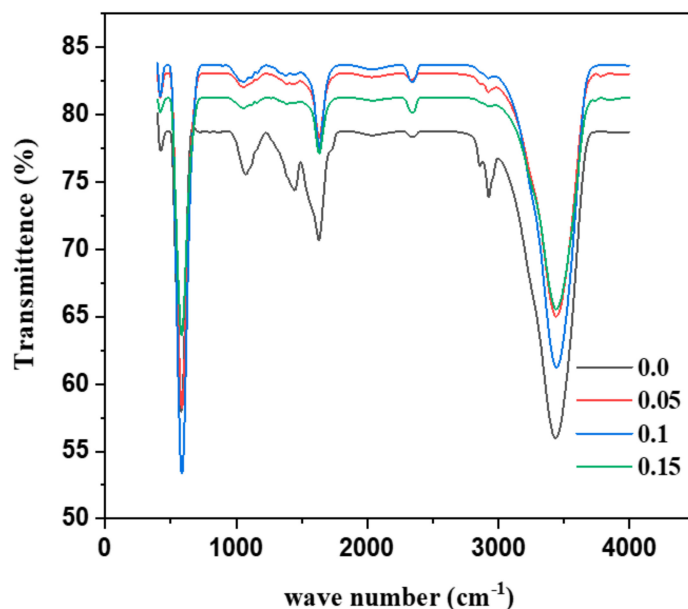


Figure 7. FTIR spectra of $\text{Co}_{0.5}\text{Zn}_{0.5}\text{Fe}_{2-x}\text{Cu}_x\text{O}_4$ ferrites.

Table 2. FTIR vibrational mode positions.

Composition	Grain Size	Vibrational Modes (ν_1)	Vibrational Modes (ν_2)
x	nm	cm^{-1}	cm^{-1}
x = 0.0	32.69	424	580
x = 0.05	21.90	421	583
x = 0.1	24.29	420	584
x = 0.15	23.72	419	586

3.4. XPS and Cationic Distribution

The XPS Zn2p, Fe2p, Co2p, Cu2p, and 1Os spectra shown in Figure 8a–d reveal the presence of Co, Zn, Fe, and Cu in the present samples, with their oxidation states and oxygen vacancies created because of the introduction of copper ions in the lattice of Co–Zn ferrite. The Co 2p spectra given in Figure 8a show two peaks at $\sim 780\text{ eV}$ and $\sim 795\text{ eV}$ associated with $\text{Co}2p_{3/2}$ and $\text{Co}2p_{1/2}$ orbitals, respectively, with the presence of two satellite peaks, which reveal that cobalt exists in a Co^{2+} oxidation state (ionic radii, $r = 0.58\text{ \AA}$) with binding energy peaks at approximately 781 eV and 796 eV , respectively. The Co^{2+} ions have a strong site preference for octahedral sites but some of them occupy the tetrahedral sites in cobalt–zinc ferrite, as reported in the literature [38]. The peaks with binding energy around 780 eV and 795 eV , respectively, are attributed to Co^{3+} oxidation states that have strong octahedral site preference and would replace Fe^{3+} ions at the octahedral site (ionic radii, $r = 0.61\text{ \AA}$) [39,40]. The deconvoluted peaks' areas under 780 eV and 781 eV correspond to the distribution of Co^{2+} ions at tetrahedral and octahedral sites, respectively, which determines the cationic distribution of cobalt ions in the lattice, similarly for other cations [32]. In Zn 2p spectra, the peaks at binding energy around 1021 eV and 1044 eV , respectively, belong to Zn $2p_{3/2}$ and Zn $2p_{1/2}$, which indicates the presence of zinc in the Zn^{2+} state, which preferably occupies tetrahedral sites (ionic radii, $r = 0.60\text{ \AA}$)

in all the samples, as observed in Figure 8d [41]. The Fe 2p spectra shown in Figure 8b show the presence of iron in Fe³⁺ (ionic radii, $r = 0.64\text{\AA}$) and Fe²⁺ oxidation states (ionic radii, $r = 0.63\text{\AA}$) [40,42,43]. The Cu 2p spectra shown in Figure 8d show the presence of copper in the Cu¹⁺ oxidation state (ionic radii, $r = 0.60\text{\AA}$); as the copper concentration increased, it was observed that it existed in the Cu²⁺ oxidation state (ionic radii, $r = 0.73\text{\AA}$), as confirmed by the strong Cu²⁺ satellite peaks [44]. Figure 8c shows that the oxygen vacancies decreased when $x = 0.05$, which was possibly due to the incorporation of Cu¹⁺ ions, and they increased with the increase in the copper concentration, which may be due to the introduction of divalent Cu ions at the tetrahedral site. The oxygen vacancies were generated to maintain charge neutrality. This was due to the substitution of Fe³⁺ ions with Cu²⁺ ions with relatively low oxidation states [45,46]. Based on the oxidation states and their corresponding ionic radii, the cationic distribution was determined for all the samples.

- (I) $\text{Co}_{0.5}\text{Zn}_{0.5}\text{Fe}_2\text{O}_4 = [\text{Zn}^{2+}_{0.5}\text{Co}^{2+}_{0.15}\text{Fe}^{3+}_{0.86}]_{\text{T}}[\text{Co}^{2+}_{0.11}\text{Co}^{3+}_{0.24}\text{Fe}^{2+}_{0.86}\text{Fe}^{3+}_{0.46}]_{\text{O}}$
 (II) $\text{Cu}_{0.05}\text{Co}_{0.5}\text{Zn}_{0.5}\text{Fe}_{1.95}\text{O}_4 = [\text{Cu}^{1+}_{0.05}\text{Zn}^{2+}_{0.5}\text{Co}^{2+}_{0.7}\text{Fe}^{3+}_{0.65}]_{\text{T}}[\text{Co}^{2+}_{0.12}\text{Co}^{3+}_{0.31}\text{Fe}^{2+}_{0.8}\text{Fe}^{3+}_{0.5}]_{\text{O}}$
 (III) $\text{Cu}_{0.1}\text{Co}_{0.5}\text{Zn}_{0.5}\text{Fe}_{1.90}\text{O}_4 = [\text{Cu}^{2+}_{0.1}\text{Zn}^{2+}_{0.5}\text{Co}^{2+}_{0.15}\text{Fe}^{3+}_{0.66}]_{\text{T}}[\text{Co}^{2+}_{0.12}\text{Co}^{3+}_{0.33}\text{Fe}^{2+}_{0.74}\text{Fe}^{3+}_{0.5}]_{\text{O}}$
 (IV) $\text{Cu}_{0.15}\text{Co}_{0.5}\text{Zn}_{0.5}\text{Fe}_{1.90}\text{O}_4 = [\text{Cu}^{2+}_{0.15}\text{Zn}^{2+}_{0.5}\text{Co}^{2+}_{0.16}\text{Fe}^{3+}_{0.63}]_{\text{T}}[\text{Co}^{2+}_{0.13}\text{Co}^{3+}_{0.33}\text{Fe}^{2+}_{0.74}\text{Fe}^{3+}_{0.63}]_{\text{O}}$

From the observed cationic distribution, it was concluded that Zn²⁺ occupied only the tetrahedral site because of its comparable ionic radius and charge. However, Co and Fe existed in 2+ and 3+ oxidation states and were preferably distributed among both A and B sites. When $x = 0.05$, the copper ions existed in the Cu¹⁺ oxidation state with an ionic radius $r = 0.60\text{\AA}$ and occupied the A site, but at relatively high concentrations, copper existed in 2+ oxidation state with ionic radius $r = 0.55\text{\AA}$ and occupied the A site.

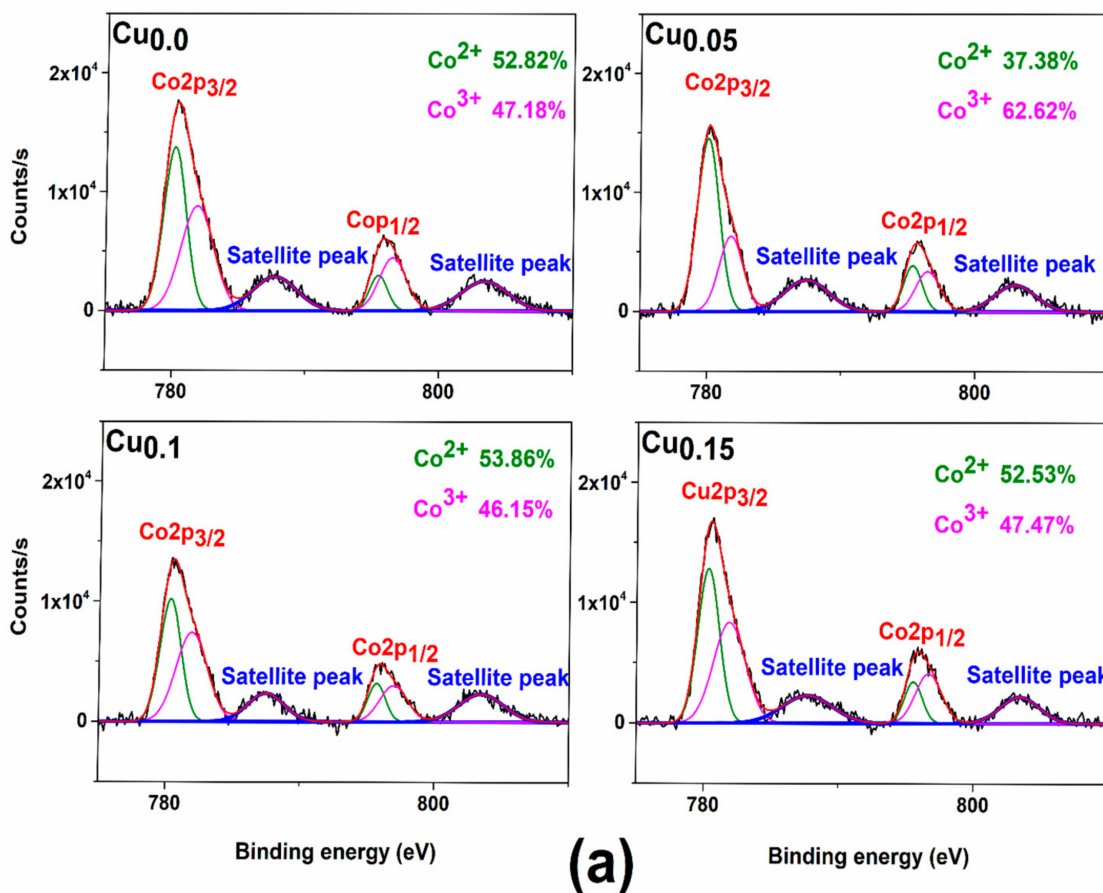


Figure 8. Cont.

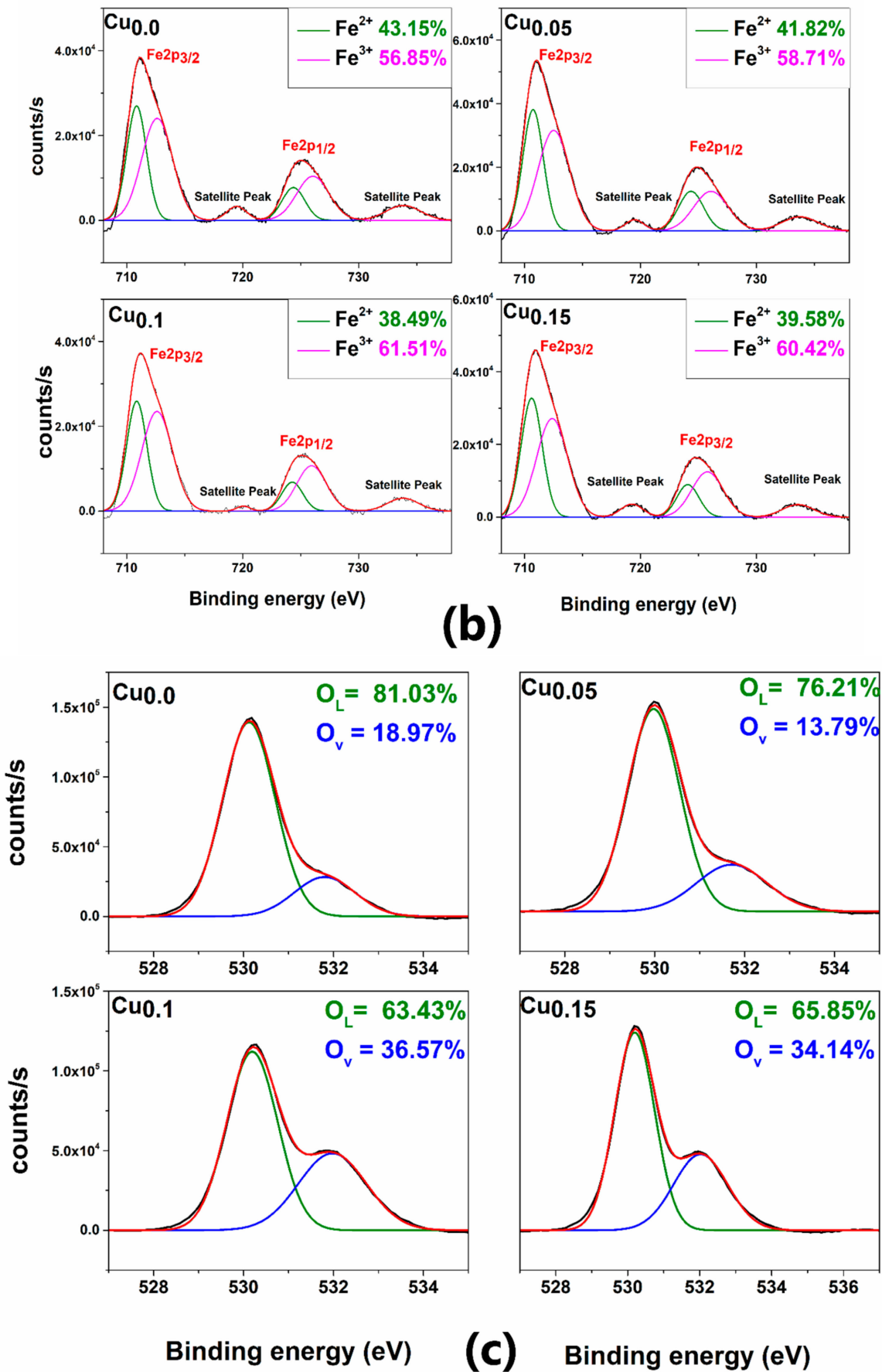


Figure 8. Cont.

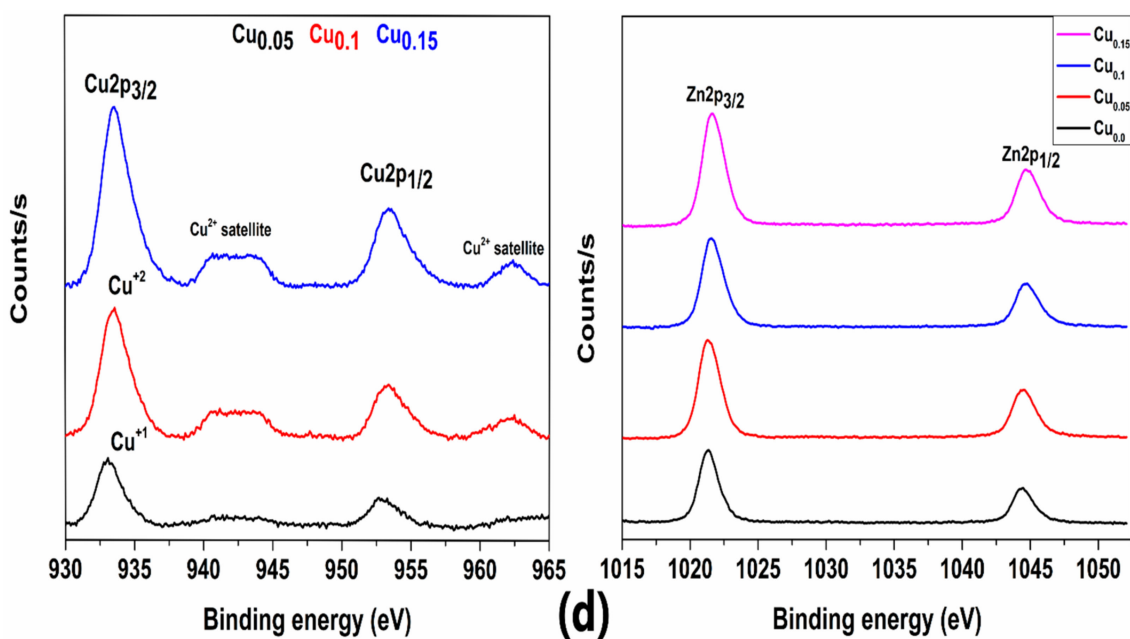


Figure 8. (a) Co2p spectra (b) Fe 2p spectra (c) O1s spectra (d) Cu2p and Zn2p spectra ($x = 0.0 - 0.15$).

3.5. Dielectric Measurement

The samples were studied for the dielectric dispersion in the frequency range from 100 Hz to 5 MHz at room temperature. Figure 9 shows the real dielectric constant (ϵ') of the prepared Cu-doped Co–Zn ferrite nanoparticles versus the frequency of the applied field. The dielectric dispersion showed the normal Maxwell–Wagner type of interfacial polarization response, where it decreases with the increase in the frequency of the applied field [47]. The graph shows that the dielectric constant decreased sharply up to 5 kHz, and thereafter, it decreased very slowly and approached saturation or showed an almost frequency-independent response. This is because, initially, the domains in a dielectric material without an externally applied field were randomly oriented and they were oriented along the direction of the field once it was applied.

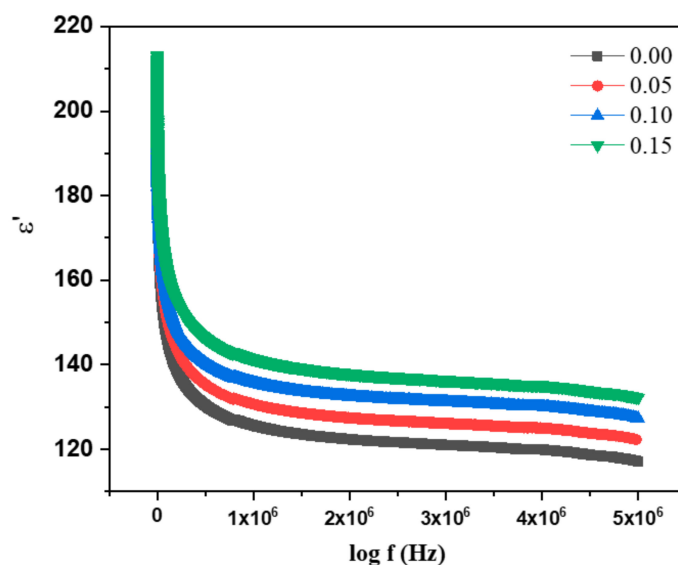


Figure 9. Variation of the real part of the dielectric constant with the frequency of $\text{Co}_{0.5}\text{Zn}_{0.5}\text{Fe}_{2-x}\text{Cu}_x\text{O}_4$ ferrites.

In the beginning, the domains aligned themselves along the direction of the applied field and they showed perfect switching response; however, as the field frequency increased further, the domains could not cope up with the frequency changes of the applied field, and hence, they lagged, which was seen above 5 kHz in the study. Furthermore, the dielectric constant increased with the increase in Cu doping, showing that the hopping of charges between the charge carriers, which was initially between Fe^{3+} and Fe^{2+} , was further supported by the hopping of charges between the Cu^{1+} and Cu^{2+} state [48].

3.6. Dielectric Loss ($\tan\delta$)

The dielectric loss is an important measurement to help determine the feasibility of any material for electrical applications, especially in capacitor materials or bridge circuits. A material with a dielectric loss less than unity is considered the best material for any electronic application, especially in MLIC technology. The dielectric loss of the copper-doped Co–Zn nanoparticles was studied in the frequency range from 100 Hz to 5 MHz and is shown in Figure 10. The dielectric loss showed a normal response for the studied applied field frequency, where it decreased with the increase in the frequency of the field. The dielectric loss was notably less than unity, and hence, this showed that the prepared material is good for high resistance applications and the fabrication of the MLIC chips [20]. The dielectric loss was observed to increase with the increase in Cu concentration, and it was the highest for the 15% doping.

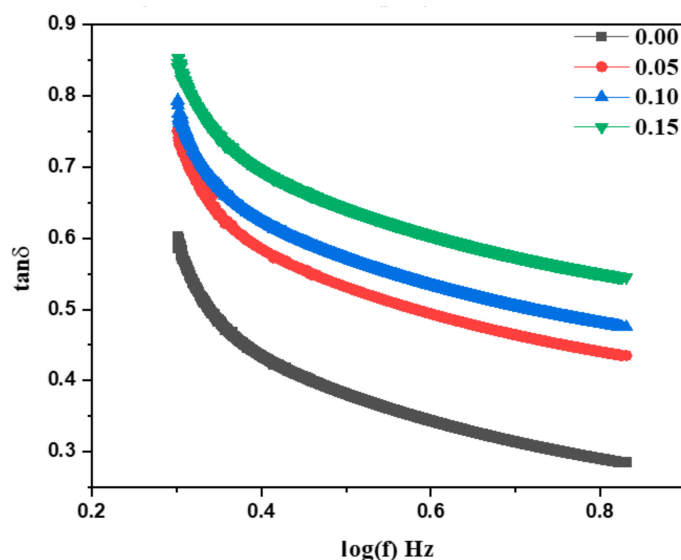


Figure 10. Shows plot of loss tangent versus frequency for $\text{Co}_{0.5}\text{Zn}_{0.5}\text{Fe}_{2-x}\text{Cu}_x\text{O}_4$ ferrites.

3.7. AC Conductivity (σ_{ac})

The AC conductivities of the as-grown copper substituted Co–Zn nanoparticles were studied in the frequency range of 100 Hz to 5 MHz at room temperature, as shown in Figure 11. The conductivity response with frequency shows the normal behavior, where it increases slowly in the low-frequency region and sharply in the high-frequency region. This can be explained with the hopping model of charges, where the hopping of charges between the charge carriers Fe^{3+} and Fe^{2+} increases with increasing frequency [49]. The hopping of charge between two Fe states is n-type while an additional type of hopping called p-type results due to the Cu doping between the two charge states of Cu^{2+} and Cu^{1+} , which also contributes to the increase in conductivity of the samples and is seen to increase with an increasing copper concentration.

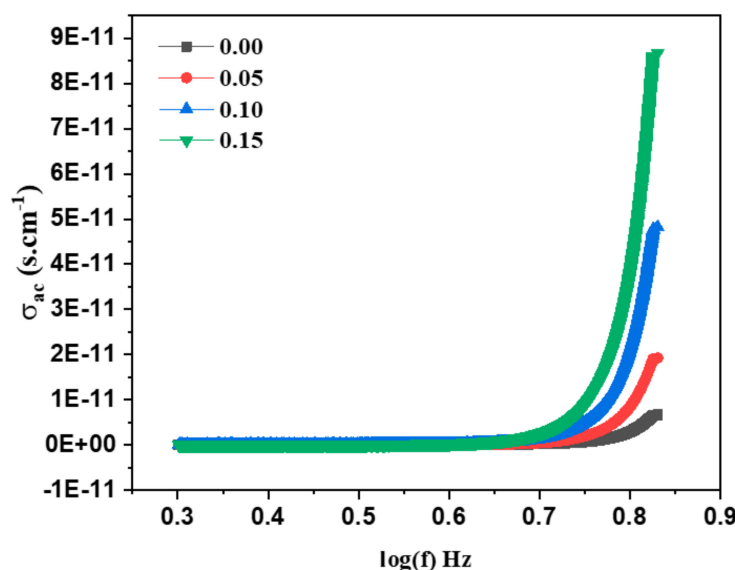


Figure 11. Shows plot AC conductivity versus frequency for $\text{Co}_{0.5}\text{Zn}_{0.5}\text{Fe}_{2-x}\text{Cu}_x\text{O}_4$ ferrites.

3.8. Magnetic Properties

The magnetic hysteresis measurement for the pure and Cu^{2+} -doped Co–Zn ferrite nanoparticles are shown in Figure 12, which reveals the ferromagnetic response of the samples. Magnetic parameters such as magnetic saturation M_s , coercivity M_H , remanence magnetization M_r , and magnetic moment η_B are listed in Table 3. The “S” shaped hysteresis loop reveals the ferromagnetic behavior of pure and Cu^{2+} -doped Co–Zn ferrite nanoparticles [50]. The variation in the M_s value can be explained by the Neel model, where the A–B exchange interactions are more predominant than those of A–A and B–B superexchange ion interactions, and the net magnetic moment of the spinel lattice is equal to the difference of the magnetic moments of the A site and B site, i.e., $M = |M_B - M_A|$ [51]. It can be seen that the saturation of magnetization M_s decreases with doping of Cu^{2+} ions, which is because the Fe^{3+} ions with magnetic moments of $5 \mu_B$ are being replaced by the Cu^{2+} ions with lower magnetic moments of $1 \mu_B$ at the tetrahedral site. However, the size of the tetrahedral site is small compared to that of the octahedral site and cannot accommodate excess copper ions. The saturation magnetization initially decreases but it increases when doping concentration is increased further, as noted when $x = 0.1$. The higher value of M_s for $x = 0.1$ can be attributed to the substitution of Cu^{2+} in the tetrahedral site where it pushes Fe^{3+} to the octahedral site and thus increases the superexchange ion interactions between Fe^{2+} and Fe^{3+} , which results in an increase in the magnetic moment at the octahedral site, and an overall increase in the net magnetic moment is observed [52,53]. When copper concentration reaches $x = 0.15$, copper ions with lower magnetic moment concentrations increase in both tetrahedral and octahedral sites and decrease the saturation of magnetization. The net magnetic moment given in Table 3 was calculated using the given formula:

$$\eta_B = \frac{M_W \times M_S}{5585} \quad (14)$$

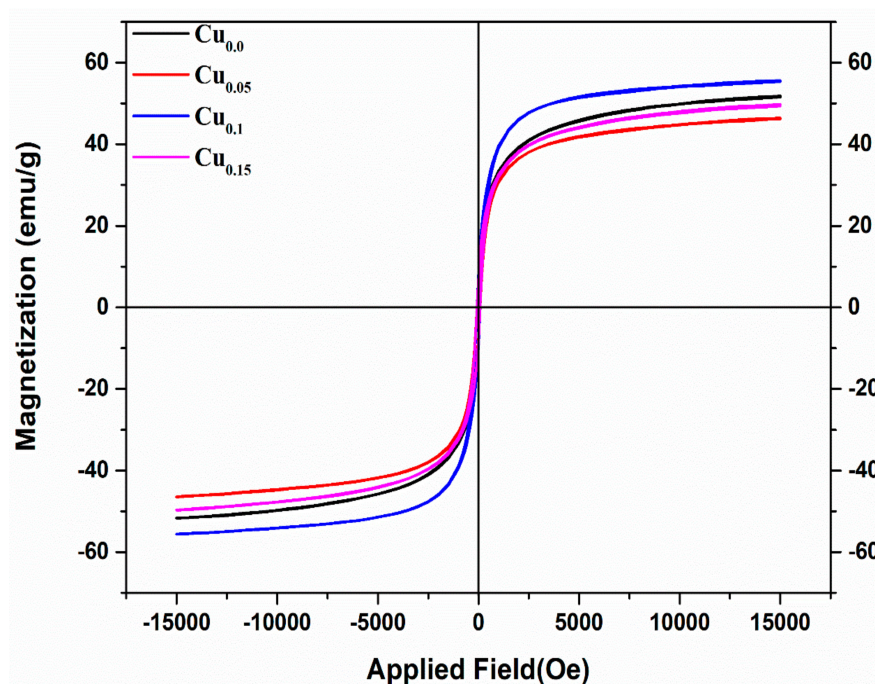


Figure 12. M versus H hysteresis loop for $\text{Co}_{0.5}\text{Zn}_{0.5}\text{Fe}_{2-x}\text{Cu}_x\text{O}_4$ ferrites.

Table 3. Magnetic parameters of the pure and Cu^{2+} cobalt–zinc ferrite.

Cu^{2+}	M_S (emu/g)	M_H (Oe)	M_R (emu/g)	K (erg/cm ³)	SQR	η_B
0.0	52.03	82.71	8.03	4482.7	0.154	2.2
0.05	46.41	79.51	7.2	3890.1	0.155	1.97
0.1	55.61	78.64	8.81	4555.3	0.112	2.37
0.15	49.47	79.39	7.81	40861.1	0.157	2.1

The incorporation of Cu^{2+} in the lattice of Co–Zn ferrite introduces the change in coercivity and magnetic anisotropic constant (K), which is listed in Table 3 and was calculated using the given equation [54]:

$$H_C = \frac{0.96K}{M_S} \quad (15)$$

The decrease in coercivity is a result of the change in the magnetic anisotropic constant, which can be due to lower magneto anisotropy of Cu^{2+} ions [55]. However, when $x = 0.1$, the copper ion present in the tetrahedral site has the lowest coercivity and highest value of magnetocrystalline anisotropy constant, which may be attributed to Jahn–Teller distortions induced by Cu^{2+} ions in the spinel ferrite system [52,54,56]. The squareness ratio (SQR) was calculated using the given formula [57]:

$$\text{SQR} = \frac{M_r}{M_S} \quad (16)$$

From Table 3 it can be seen that the squareness ratio is less than 0.5, which proves the samples have uniaxial anisotropy rather than cubic anisotropy. The lower value of the SQR contributes to the application of the ferrites for high-frequency applications [55,58,59].

4. Conclusions

Single-phase cubic spinel ferrites of Cu-doped Co–Zn ferrite nanoparticles with average crystallite sizes ranging between 20.57 nm and 32.69 nm, as confirmed by the XRD analysis, were successfully synthesized using the sol–gel auto-combustion technique. The

W–H plot revealed that a uniform strain developed in all directions at all doping concentrations of Cu. The TEM micrographs confirmed the polycrystalline nature of the samples when Cu = 0.0 and 0.05, and EDS revealed the elemental composition of both the samples without any impurity phases. FTIR studies showed the presence of two prominent peaks at approximately 420 cm^{-1} and 580 cm^{-1} , showing metal–oxygen stretching and the formation of ferrite composite. The XPS revealed the oxidation states of the elements present in the ferrite samples. Based on the corresponding ionic radii of different oxidation states and the calculated ionic radii for the cations of the tetrahedral and octahedral sites, the cationic distribution was proposed. The dielectric spectroscopy showed that samples exhibited Maxwell–Wagner interfacial polarization, which decreased as the frequency of the applied field increased. The dielectric loss of the samples was less than 1, confirming that the samples can be used to fabricate MLICs. The AC conductivity of the samples increased with the increase in doping and with frequency, and this was explained based on the hopping model. Magnetic studies showed that the samples exhibit ferromagnetic properties and have uniaxial anisotropy rather than cubic anisotropy. The low value of the squareness ratio further suggests that the samples are a good choice for high-frequency applications.

Author Contributions: Funding acquisition, K.M.B.; Investigation, M.H. and A.C.; Methodology, K.M.B.; Project administration, R.V.; Resources, Y.Y.; Supervision, K.M.B. and O.M.A.; Writing—original draft, M.H., K.M.B. and A.C. All authors have read and agreed to the published version of the manuscript.

Funding: Deanship of Scientific research (DSR) provided the funding for this research work under the initiative of DSR (graduate students Research support).

Data Availability Statement: The data presented in this study are available within the article.

Acknowledgments: The authors would like to thank the Deanship of scientific research at King Saud University for funding and supporting this research through the initiative of DSR (graduate students Research Support).

Conflicts of Interest: The authors declare no conflict of interest.

References

1. Lisiecki, I.; Pileni, M.P. Synthesis of copper metallic clusters using reverse micelles as microreactors. *J. Am. Chem. Soc.* **1993**, *115*, 3887–3896. [[CrossRef](#)]
2. Petit, C.; Lixon, P.; Pileni, M.P. In situ synthesis of silver nanocluster in AOT reverse micelles. *J. Phys. Chem.* **1993**, *97*, 12974–12983. [[CrossRef](#)]
3. Gubbala, S.; Nathani, H.; Koizol, K.; Misra, R.D.K. Magnetic properties of nanocrystalline Ni–Zn, Zn–Mn, and Ni–Mn ferrites synthesized by reverse micelle technique. *Phys. B Condens. Matter* **2004**, *348*, 317–328. [[CrossRef](#)]
4. Berkowitz, E.A.; Schuele, J.W. Magnetic properties of some ferrite micropowders. *J. Appl. Phys.* **1959**, *30*, S134–S135. [[CrossRef](#)]
5. Lee, J.G.; Park, J.Y.; Oh, Y.J.; Kim, C.S. Magnetic properties of CoFe₂O₄ thin films prepared by a sol-gel method. *J. Appl. Phys.* **1998**, *84*, 2801–2804. [[CrossRef](#)]
6. el Foulani, A.H.; Aamouche, A.; Mohseni, F.; Amaral, J.S.; Tobaldi, D.M.; Pullar, R.C. Effect of surfactants on the optical and magnetic properties of cobalt-zinc ferrite Co_{0.5}Zn_{0.5}Fe₂O₄. *J. Alloy. Compd.* **2019**, *774*, 1250–1259. [[CrossRef](#)]
7. Yousefi, M.H.; Manouchehri, S.; Arab, A.; Mozaffari, M.; Amiri, G.R.; Amighian, J. Preparation of cobalt–zinc ferrite (Co_{0.8}Zn_{0.2}Fe₂O₄) nanopowder via combustion method and investigation of its magnetic properties. *Mater. Res. Bull.* **2010**, *45*, 1792–1795. [[CrossRef](#)]
8. Tirosh, E.; Shemer, G.; Markovich, G. Optimizing cobalt ferrite nanocrystal synthesis using a magneto-optical probe. *Chem. Mater.* **2006**, *18*, 465–470. [[CrossRef](#)]
9. Iatridi, Z.; Vamvakidis, K.; Tsougos, I.; Vassiou, K.; Dendrinou-Samara, C.; Bokias, G. Multifunctional polymeric platform of magnetic ferrite colloidal superparticles for luminescence, imaging, and hyperthermia applications. *ACS Appl. Mater. Interfaces* **2016**, *8*, 35059–35070. [[CrossRef](#)]
10. Gu, H.; Xu, K.; Yang, Z.; Chang, C.K.; Xu, B. Synthesis and cellular uptake of porphyrin decorated iron oxide nanoparticles—a potential candidate for bimodal anticancer therapy. *Chem. Commun.* **2005**, *34*, 4270–4272. [[CrossRef](#)]
11. Lüders, U.; Barthelémy, A.; Bibes, M.; Bouzehouane, K.; Fusil, S.; Jacquet, E.; Contour, J.P.; Bobo, J.F.; Fontcuberta, J.; Fert, A. NiFe₂O₄: A versatile spinel material brings new opportunities for spintronics. *Adv. Mater.* **2006**, *18*, 1733–1736. [[CrossRef](#)]

12. Baldi, G.; Bonacchi, D.; Innocenti, C.; Lorenzi, G.; Sangregorio, C. Cobalt ferrite nanoparticles: The control of the particle size and surface state and their effects on magnetic properties. *J. Magn. Magn. Mater.* **2007**, *311*, 10–16. [CrossRef]
13. Halder, S.; Liba, S.I.; Nahar, A.; Sikder, S.S.; Hoque, S.M. To study the surface modified cobalt zinc ferrite nanoparticles for application to magnetic hyperthermia. *AIP Adv.* **2020**, *10*, 125308. [CrossRef]
14. Feng, J.; Xiong, R.; Liu, Y.; Su, F.; Zhang, X. Preparation of cobalt substituted zinc ferrite nanopowders via auto-combustion route: An investigation to their structural and magnetic properties. *J. Mater. Sci. Mater. Electron.* **2018**, *29*, 18358–18371. [CrossRef]
15. Köseoğlu, Y.; Baykal, A.; Gözüak, F.A.; Kavas, H.Ü. Structural and magnetic properties of $\text{Co}_x\text{Zn}_{1-x}\text{Fe}_2\text{O}_4$ nanocrystals synthesized by microwave method. *Polyhedron* **2009**, *28*, 2887–2892. [CrossRef]
16. Tang, X.X.; Manthiram, A.; Goodenough, J.B. Copper ferrite revisited. *J. Solid State Chem.* **1989**, *79*, 250–262. [CrossRef]
17. Mahalakshmi, S.; Manja, K.S.; Nithyanantham, S. Structural and morphological studies of copper-doped nickel ferrite. *J. Supercond. Nov. Magn.* **2015**, *28*, 3093–3098. [CrossRef]
18. Ghosh, M.P.; Datta, S.; Sharma, R.; Tanbir, K.; Kar, M.; Mukherjee, S. Copper doped nickel ferrite nanoparticles: Jahn-Teller distortion and its effect on microstructural, magnetic and electronic properties. *Mater. Sci. Eng. B* **2021**, *263*, 114864.
19. Köppel, H.; Yarkony, D.R.; Barentzen, H. (Eds.) *The Jahn-Teller Effect: Fundamentals and Implications for Physics and Chemistry*; Springer Science & Business Media: Berlin/Heidelberg, Germany, 2009; Volume 97.
20. Villette, C.; Tailhades, P.; Rousset, A. Thermal behavior and magnetic properties of acicular copper-cobalt ferrite particles. *J. Solid State Chem.* **1995**, *117*, 64–72. [CrossRef]
21. Kargar, Z.; Asgarian, S.M.; Mozaffari, M. Positron annihilation and magnetic properties studies of copper substituted nickel ferrite nanoparticles. *Nucl. Instrum. Methods Phys. Res. Sect. B Beam Interact. Mater. At.* **2016**, *375*, 71–78. [CrossRef]
22. Humbe, A.V.; Nawle, A.C.; Shinde, A.B.; Jadhav, K.M. Impact of Jahn Teller ion on magnetic and semiconducting behaviour of Ni-Zn spinel ferrite synthesized by nitrate-citrate route. *J. Alloy. Compd.* **2017**, *691*, 343–354. [CrossRef]
23. Batoo, K.M.; Ansari, M.S. Low temperature-fired Ni-Cu-Zn ferrite nanoparticles through auto-combustion method for multilayer chip inductor applications. *Nanoscale Res. Lett.* **2012**, *7*, 1–14. [CrossRef]
24. Qindeel, R.; Alonizan, N.H. Structural, dielectric and magnetic properties of cobalt based spinel ferrites. *Curr. Appl. Phys.* **2018**, *18*, 519–525. [CrossRef]
25. Sujatha, C.; Reddy, K.V.; Babu, K.S.; Reddy, A.R.; Rao, K.H. Structural and magnetic properties of $\text{Ni}_{0.5-x}\text{Mg}_x\text{Cu}_{0.05}\text{Zn}_{0.45}\text{Fe}_2\text{O}_4$ ferrites for multilayer chip inductor applications. In *International Conference on Nanoscience, Engineering and Technology (ICONSET 2011)*; IEEE: New York, NY, USA, 2011; pp. 19–22.
26. Radoń, A.; Hawelek, Ł.; Łukowiec, D.; Kubacki, J.; Włodarczyk, P. Dielectric and electromagnetic interference shielding properties of high entropy (Zn, Fe, Ni, Mg, Cd) Fe_2O_4 ferrite. *Sci. Rep.* **2019**, *9*, 1–13. [CrossRef]
27. Xie, J.; Han, M.; Chen, L.; Kuang, R.; Deng, L. Microwave-absorbing properties of NiCoZn spinel ferrites. *J. Magn. Magn. Mater.* **2007**, *314*, 37–42. [CrossRef]
28. Gurusiddesh, M.; Madhu, B.J.; Shankaramurthy, G.J. Structural, dielectric, magnetic and electromagnetic interference shielding investigations of polyaniline decorated $\text{Co}_{0.5}\text{Ni}_{0.5}\text{Fe}_2\text{O}_4$ nanoferrites. *J. Mater. Sci. Mater. Electron.* **2018**, *29*, 3502–3509. [CrossRef]
29. Sulaiman, J.M.; Ismail, M.M.; Rafeeq, S.N.; Mandal, A. Enhancement of electromagnetic interference shielding based on $\text{Co}_{0.5}\text{Zn}_{0.5}\text{Fe}_2\text{O}_4$ /PANI-PTSA nanocomposites. *Appl. Phys. A* **2020**, *126*, 1–9. [CrossRef]
30. Brinker, C.J.; Scherer, G.W. *Sol.-Gel Science: The Physics and Chemistry of Sol.-Gel Processing*; Academic Press: Cambridge, MA, USA, 2013.
31. Patil, V.G.; Shirsath, S.E.; More, S.D.; Shukla, S.J.; Jadhav, K.M. Effect of zinc substitution on structural and elastic properties of cobalt ferrite. *J. Alloy. Compd.* **2009**, *488*, 199–203. [CrossRef]
32. A.D.S. Blog, Publication: Journal of Molecular Structure Pub Date: February 2018. Available online: <https://ui.adsabs.harvard.edu/abs/2017JMoSt1147..697./abstract> (accessed on 1 April 2021).
33. Anjum, S.; Sehar, F.; Awan, M.S.; Zia, R. Role of Bi 3+ substitution on structural, magnetic and optical properties of cobalt spinel ferrite. *Appl. Phys. A* **2016**, *122*, 436. [CrossRef]
34. Zhang, C.F.; Zhong, X.C.; Yu, H.Y.; Liu, Z.W.; Zeng, D.C. Effects of cobalt doping on the microstructure and magnetic properties of Mn-Zn ferrites prepared by the co-precipitation method. *Phys. B Condens. Matter* **2009**, *404*, 2327–2331. [CrossRef]
35. Yadav, R.S.; Kuřitka, I.; Vilcakova, J.; Havlica, J.; Masilko, J.; Kalina, L.; Tkacz, J.; Švec, J.; Enev, V.; Hajdúchová, M. Impact of grain size and structural changes on magnetic, dielectric, electrical, impedance and modulus spectroscopic characteristics of CoFe_2O_4 nanoparticles synthesized by honey mediated sol-gel combustion method. *Adv. Nat. Sci. Nanosci. Nanotechnol.* **2017**, *8*, 045002.
36. Debnath, S.; Deb, K.; Saha, B.; Das, R. X-ray diffraction analysis for the determination of elastic properties of zinc-doped manganese spinel ferrite nanocrystals ($\text{Mn}_{0.75}\text{Zn}_{0.25}\text{Fe}_2\text{O}_4$), along with the determination of ionic radii, bond lengths, and hopping lengths. *J. Phys. Chem. Solids* **2019**, *134*, 105–114. [CrossRef]
37. Mugutkar, A.B.; Gore, S.K.; Mane, R.S.; Batoo, K.M.; Adil, S.F.; Jadhav, S.S. Magneto-structural behaviour of Gd doped nanocrystalline Co-Zn ferrites governed by domain wall movement and spin rotations. *Ceram. Int.* **2018**, *44*, 21675–21683. [CrossRef]
38. Asiri, S.; Sertkol, M.; Guner, S.; Gungunes, H.; Batoo, K.M.; Saleh, T.A.; Sozeri, H.; Almessiere, M.A.; Manikandan, A.; Baykal, A. Hydrothermal synthesis of $\text{Co}_y\text{Zn}_{1-2y}\text{Fe}_2\text{O}_4$ nanoferrites: Magneto-optical investigation. *Ceram. Int.* **2018**, *44*, 5751–5759.
39. Qamar, S.; Akhtar, M.N.; Batoo, K.M.; Raslan, E.H. Structural and magnetic features of Ce doped Co-Cu-Zn spinel nanoferrites prepared using sol gel self-ignition method. *Ceram. Int.* **2020**, *46*, 14481–14487. [CrossRef]

40. Markova-Deneva, I. Infrared spectroscopy investigation of metallic nanoparticles based on copper, cobalt, and nickel synthesized through borohydride reduction method. *J. Univ. Chem. Technol. Metall.* **2010**, *45*, 351–378.
41. Veverka, M.; Jiráček, Z.; Kaman, O.; Knížek, K.; Maryško, M.; Pollert, E.; Závěta, K.; Lančok, A.; Dlouhá, M.; Vratislav, S. Distribution of cations in nanosize and bulk Co–Zn ferrites. *Nanotechnology* **2011**, *22*, 345701. [[CrossRef](#)]
42. Murray, P.J.; Linnett, J.W. Cation distribution in the spinels $\text{Co}_x\text{Fe}_{3-x}\text{O}_4$. *J. Phys. Chem. Solids* **1976**, *37*, 1041–1042. [[CrossRef](#)]
43. Bennet, J.; Tholkappiyan, R.; Vishista, K.; Jaya, N.V.; Hamed, F. Attestation in self-propagating combustion approach of spinel AFe_2O_4 (A = Co, Mg and Mn) complexes bearing mixed oxidation states: Magnetostructural properties. *Appl. Surf. Sci.* **2016**, *383*, 113–125. [[CrossRef](#)]
44. Vinuthna, C.H.; Chandra Babu Naidu, K.; Dachepalli, R. Magnetic and antimicrobial properties of cobalt-zinc ferrite nanoparticles synthesized by citrate-gel method. *Int. J. Appl. Ceram. Technol.* **2019**, *16*, 1944–1953.
45. Wang, W.P.; Yang, H.; Xian, T.; Jiang, J.L. XPS and magnetic properties of CoFe_2O_4 nanoparticles synthesized by a polyacrylamide gel route. *Mater. Trans.* **2012**, *53*, 1586–1589. [[CrossRef](#)]
46. Shannon, R.T.; Prewitt, C.T. Revised values of effective ionic radii. *Acta Crystallogr. Sect. B Struct. Crystallogr. Cryst. Chem.* **1970**, *26*, 1046–1048. [[CrossRef](#)]
47. Zhang, H.; Li, C.; Lyu, L.; Hu, C. Surface oxygen vacancy inducing peroxymonosulfate activation through electron donation of pollutants over cobalt-zinc ferrite for water purification. *Appl. Catal. B Environ.* **2020**, *270*, 118874. [[CrossRef](#)]
48. Muthukumar, K.; Lakshmi, D.S.; Acharya, S.D.; Natarajan, S.; Mukherjee, A.; Bajaj, H.C. Solvothermal synthesis of magnetic copper ferrite nano sheet and its antimicrobial studies. *Mater. Chem. Phys.* **2018**, *209*, 172–179. [[CrossRef](#)]
49. Jauhar, S.; Singhal, S. Substituted cobalt nano-ferrites, $\text{Co}_m\text{Fe}_{2-x}\text{O}_4$ (M = Cr^{3+} , Ni^{2+} , Cu^{2+} , Zn^{2+} ; $0.2 \leq x \leq 1.0$) as heterogeneous catalysts for modified Fenton's reaction. *Ceram. Int.* **2014**, *40*, 11845–11855. [[CrossRef](#)]
50. Yu, R.; Zhao, J.; Zhao, Z.; Cui, F. Copper substituted zinc ferrite with abundant oxygen vacancies for enhanced ciprofloxacin degradation via peroxymonosulfate activation. *J. Hazard. Mater.* **2020**, *390*, 121998. [[CrossRef](#)]
51. Batoo, K.M.; Kumar, S.; Lee, C.G. Influence of Al doping on electrical properties of Ni–Cd nano ferrites. *Curr. Appl. Phys.* **2009**, *9*, 826–832. [[CrossRef](#)]
52. Hashim, M.; Kumar, S.; Koo, B.H.; Shirsath, S.E.; Mohammed, E.M.; Shah, J.; Kotnala, R.K.; Choi, H.K.; Chung, H.; Kumar, R. Structural, electrical and magnetic properties of Co–Cu ferrite nanoparticles. *J. Alloy. Compd.* **2012**, *518*, 11–18. [[CrossRef](#)]
53. Batoo, K.M.; Kumar, G.; Yang, Y.; Al-Douri, Y.; Singh, M.; Jotania, R.B.; Imran, A. Structural, morphological and electrical properties of Cd^{2+} doped $\text{MgFe}_2\text{-xO}_4$ ferrite nanoparticles. *J. Alloy. Compd.* **2017**, *726*, 179–186. [[CrossRef](#)]
54. Batoo, K.M.; Raslan, E.H.; Yang, Y.; Adil, S.F.; Khan, M.; Imran, A.; Al-Douri, Y. Structural, dielectric and low temperature magnetic response of Zn doped cobalt ferrite nanoparticles. *AIP Adv.* **2019**, *9*, 055202. [[CrossRef](#)]
55. Rao, P.A.; Rao, K.S.; Raju, T.P.; Kapusetti, G.; Choppadandi, M.; Varma, M.C.; Rao, K.H. A systematic study of cobalt-zinc ferrite nanoparticles for self-regulated magnetic hyperthermia. *J. Alloy. Compd.* **2019**, *794*, 60–67.
56. Asgarian, S.M.; Pourmasoud, S.; Kargar, Z.; Sobhani-Nasab, A.; Eghbali-Arani, M. Investigation of positron annihilation lifetime and magnetic properties of $\text{Co}_{1-x}\text{Cu}_x\text{Fe}_2\text{O}_4$ nanoparticles. *Mater. Res. Express* **2018**, *6*, 015023. [[CrossRef](#)]
57. Tedjiekeng, H.M.K.; Tsobnang, P.K.; Fomekong, R.L.; Etape, E.P.; Joy, P.A.; Delcorte, A.; Lambi, J.N. Structural characterization and magnetic properties of undoped and copper-doped cobalt ferrite nanoparticles prepared by the octanoate coprecipitation route at very low dopant concentrations. *RSC Adv.* **2018**, *8*, 38621–38630. [[CrossRef](#)]
58. Baykal, A.; Guner, S.; Gungunes, H.; Batoo, K.M.; Amir, M.; Manikandan, A. Magneto optical properties and hyperfine interactions of Cr^{3+} ion substituted copper ferrite nanoparticles. *J. Inorg. Organomet. Polym. Mater.* **2018**, *28*, 2533–2544. [[CrossRef](#)]
59. Jiang, N.N.; Yang, Y.; Zhang, Y.X.; Zhou, J.P.; Liu, P.; Deng, C.Y. Influence of zinc concentration on structure, complex permittivity and permeability of Ni–Zn ferrites at high frequency. *J. Magn. Magn. Mater.* **2016**, *401*, 370–377. [[CrossRef](#)]